Energy Storage Materials 21 (2019) 97–106

Contents lists available at ScienceDirect

Energy Storage Materials

journal homepage: www.elsevier.com/locate/ensm

Hierarchical mesoporous $MoSe_2$@CoSe/N-doped carbon nanocomposite for sodium ion batteries and hydrogen evolution reaction applications

Jing Chen[a], Anqiang Pan[a,*], Yaping Wang[a], Xinxin Cao[a], Wenchao Zhang[b], Xiangzhong Kong[a], Qiong Su[a], Jiande Lin[a], Guozhong Cao[c,*], Shuquan Liang[a,*]

[a] School of Materials Science & Engineering, Central South University, Changsha, Hunan 410083, China
[b] Institute for Superconducting & Electronic Materials, School of Mechanical, Materials, Mechatronics & Biomedical Engineering, Faculty of Engineering and Information Sciences, University of Wollongong, NSW 2500, Australia
[c] Department of Materials Science & Engineering, University of Washington, Seattle, WA 98195, USA

ARTICLE INFO

Keywords:
Hierarchical mesoporous structure
Heterostructure
$MoSe_2$@CoSe/N-C
Sodium-ion batteries
Hydrogen evolution reaction

ABSTRACT

$MoSe_2$ has been attracting numerous attentions for energy storage and conversion applications due to its unique characteristics. However, the intrinsic low electric conductivity and sluggish reaction kinetics hinder its electrochemical performance. Herein, hierarchical mesoporous $MoSe_2$@CoSe/N-doped carbon (N-C) composite was in situ fabricated from MoO_3@Co-MOF precursor in selenium atmosphere. The incorporation of CoSe and N-C greatly enhanced the reaction kinetics and electronic conductivity of the composite. Moreover, the hierarchical mesoporous structure ensures fast Na^+ diffusion and excellent structural stability upon cycling. As expected, the optimally structured composite showed superior electrochemical performance as an anode material in sodium-ion batteries, including a high specific capacity of 485 mA h g^{-1} at 0.1 A g^{-1} and good rate capability that it retains 91.4% of its 398 mA h g^{-1} initial capacity after 300 cycles at 2 A g^{-1}. When paired with $Na_3V_2(PO_4)_3$/C, it also delivers a high reversible capacity of 345 mA h g^{-1} in full-cell configuration. In addition, as a catalyst, it also exhibits outstanding HER activity with a small overpotential of 64 mV and a Tafel slope of 53 mV dec^{-1}.

1. Introduction

The surging demand of energy has accelerated the development of clean and sustainable energy technologies in recent years [1–3]. Sodium-ion batteries (SIBs) and hydrogen production through electrocatalytic hydrogen evolution reaction have stood out due to their highly abundant raw materials and low pollution [4–6]. Recently, the transition metal chalcogenides have attracted great attention as electrode materials and catalysts because of their high reversible capacity, appropriate working potential and inherent HER activity [7–10]. Among them, transition metal selenides, including $MoSe_2$ and CoSe, are outstanding thanks to their higher conductivity than the corresponding oxides and sulfides as Se brings its intrinsic metallic nature [11–14]. The sandwich structure of them, with the metal atom layer between two selenium layers, was stacked by weak van der Waals forces [11,15]. Such a unique structure confers various favorable properties: easy interlayer expansion for accommodating Na^+ ions and exposed edges for better catalytic activity [16–22]. However, these two dimensional materials tend to restack and aggregate, which impairs their performance in many practical applications [23–25]. The large volume change of these materials during electrochemical reactions also leads to limited cycling stability [26,27].

To address these issues, designing hierarchical porous nanostructured materials with high surface area has been regarded as an efficient approach [28,29]. The nanoscale building blocks not only enlarge the contact area between electrode and electrolyte, but also provide more surface active sites [30,31]. And the porous structure can effectively accommodate the volume expansion during repeated sodiation–desodiation. It is believed that their nanosized subunits and unique architecture can enlarge merits/functions of materials [30,32,33]. For example, Xu et al. synthesized hierarchical nanotubes consist of few-layered $MoSe_2$ nanosheets, which exhibit much higher capacity and stability in SIBs [34].

On the other hand, synthesizing nanocomposites with selected components is an effective way to improve electrochemical performance due to their versatile functionalities and synergistic advantages [35,36]. Recently, to enhance the electrochemical performance of $MoSe_2$, various materials have been employed to form hybrids or

* Corresponding authors.
E-mail addresses: pananqiang@csu.edu.cn (A. Pan), gzcao@u.washington.edu (G. Cao), lsq@csu.edu.cn (S. Liang).

https://doi.org/10.1016/j.ensm.2018.10.019
Received 23 August 2018; Received in revised form 7 October 2018; Accepted 24 October 2018
Available online 26 October 2018

nanocomposites with $MoSe_2$ [37–40]. Compared to $MoSe_2$, Cobalt selenide (CoSe) exhibits relatively faster surface-controlled kinetics but inferior electrochemical stability [41]. In this regard, the combination of $MoSe_2$ and CoSe into rationally designed nanocomposite may bring synergistic advantages [39]. However, the intrinsic conductivity of $MoSe_2$/CoSe composite is still not high enough to realize fast reaction kinetics, which leads to poor rate performance and sluggish H_2 production [35,42]. To address this issue, the most commonly used strategy is to introduce carbon into the nanocomposites [13,43–46]. In particular, metal–organic frameworks (MOFs) provide a direct and facile approach to uniformly wrap metal selenides up with an in-situ formed carbon matrix. And the derived carbon matrix contains in-situ doped nitrogen which can even further improve the conductivity of the as-formed carbon network [47–49]. For example, Pan et al. have synthesized Nitrogen-Doped CoSe/C mesoporous dodecahedra with enhanced cycling stability and high rate capability [50]. Thus, by combining the advantages of hierarchical porous nanostructures and nanocomposites with high electrical conductivity, enhanced sodium storage properties and HER performance of electrode materials are highly expected. However, synthesis of such hybrid metal selenides with well-designed morphology is still challenging.

Herein, hierarchical porous $MoSe_2$@CoSe/N-doped carbon tri-composite was first controllably synthesized by selenizing cobalt-based zeolite-type MOF cladding MoO_3 nanorods, as shown in Scheme 1. The Co-MOF can produce both CoSe and N-doped carbon simultaneously and uniformly in the composite, realizing enhanced reaction kinetics and conductivity. As expected, the composite shows enhanced electrochemical performance in both SIBs and HER thanks to the synergistic advantages. Moreover, the micromorphology of as-synthesized composites can be tuned by simply changing the time duration of growing Co-MOF and a hollow and porous interior was successfully obtained. The formation of porous structure is based on the Kirkendall effect, in which MoO_3 serves as a self-sacrificing template and the CoSe/N-C act as a buffer shell of Se atmosphere. The hierarchical and mesoporous structure endows the $MoSe_2$@CoSe/N-C with greatly enhanced rate capability and cycling stability, compared to its counterparts.

2. Results and discussion

2.1. Formation mechanism and structure characterization of materials

Scheme 1 illustrates the processes of fabricating N-doped $MoSe_2$@CoSe/C nanostructured materials (details can be seen in Supporting information). MoO_3 nanorods synthesized via a facile hydrothermal process was used as the hard templates for Co-MOF growth during step I and self-sacrificing template to synthesize $MoSe_2$ during selenylation process. The growth of Co-MOF was done by simply immersing MoO_3 nanorods into the solution of 2-methylimidazole and cobalt nitrate hexahydrate at room temperature (step I). To investigate the time effect on the micro-morphology of final products, different growth durations (1 h, 3 h, 6 h and 12 h) were selected. Then, the as-prepared MoO_3@Co-MOF hybrid nanostructured precursor was reacted with selenium powder under Ar/H_2 (95%/5%) atmosphere at 700 °C for 3 h to form a mesoporous hierarchical nanostructured $MoSe_2$@CoSe/N-doped C composite.

Fig. S1 shows FT-IR spectrums of MoO_3 nanorods and MoO_3@Co-MOF samples derived from different growth time of Co-MOFs. Based on the analysis of peaks in these samples (see in Supporting information), except for peaks of MoO_3, the remaining peaks in the precursors belong to Co-MOF, and the longer the growth time of Co-MOF, the more obvious the corresponding characteristic peaks, confirming the successful formation of Co-MOF/MoO_3 composites. Moreover, the presence of Co-MOF was also confirmed by the X-ray diffraction (XRD) patterns. As revealed in Fig. S2, all the diffraction peaks of the MC-X (X = 1,3,6 and 12) samples consisted of diffraction peaks of pure MoO_3 and Co-MOF. To figure out how are these two phases distributed in the as-prepared composites, scanning electron microscope (SEM) techniques are employed. Fig. S3a shows that the pristine MoO_3 nanorods have an average width of about 300 nm and a smooth surface. MC-X samples (Fig. S3b-e) show similar morphology and no traditional ZIF-67 framework of polyhedral morphology was observed. Given that both FT-IR and XRD results suggest that MC-X are composites consist of MoO_3 and Co-MOF, while SEM result reveals

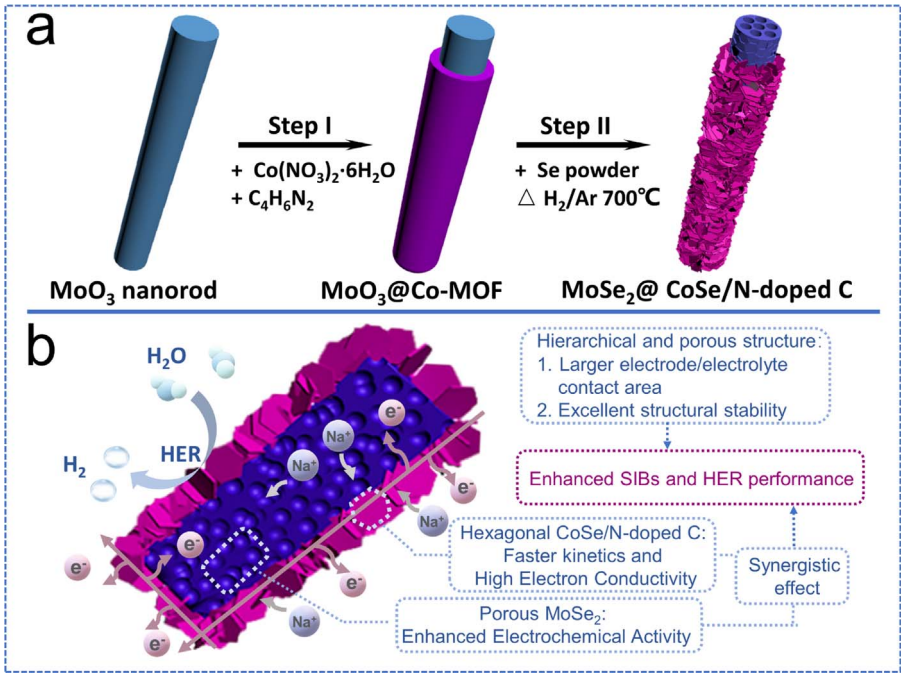

Scheme 1. (a) Illustration of the synthetic process of hierarchical $MoSe_2$@CoSe/N-doped C: (I) growth of Co-MOF on MoO_3 nanorods and (II) in situ synthesis of $MoSe_2$@CoSe/N-doped C with selenium powder; (b) Schematic illustration of $MoSe_2$@CoSe/N-doped C as an electrode material towards sodium Ion batteries (SIBs) and hydrogen evolution reaction (HER).

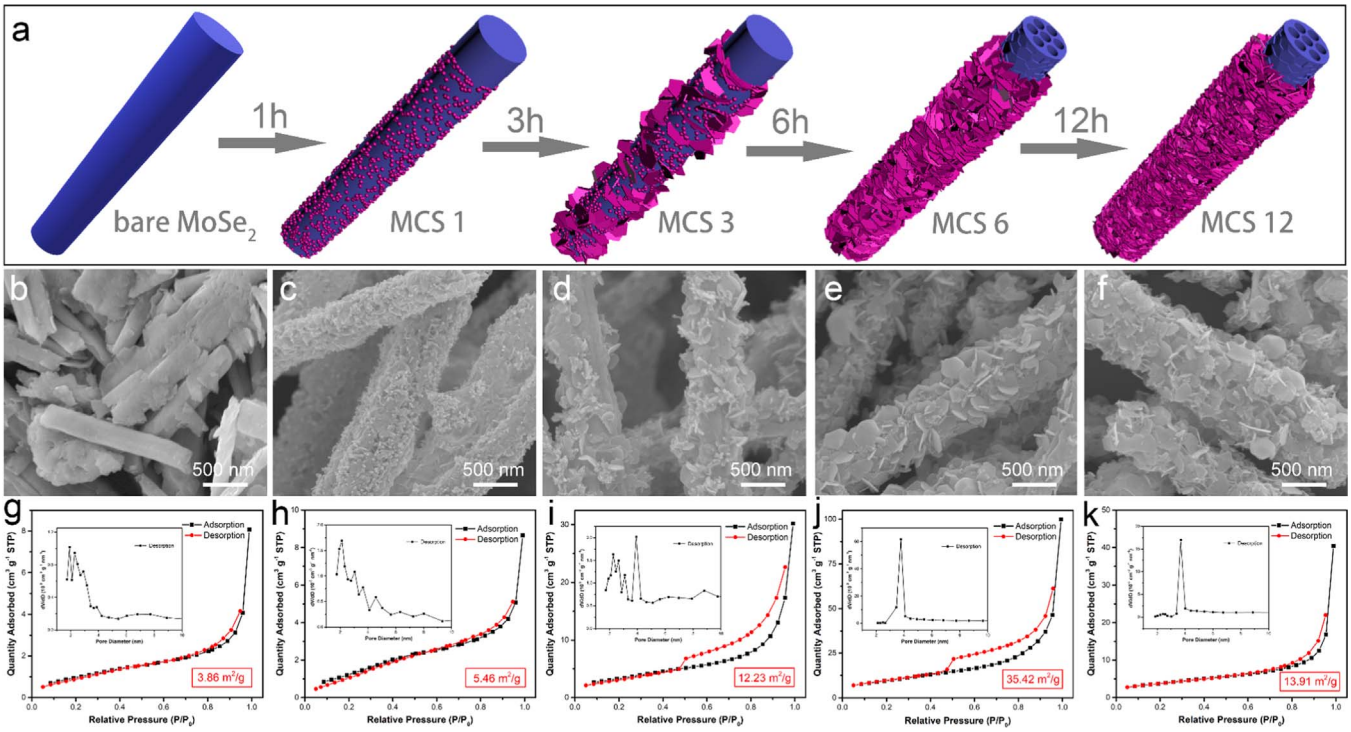

Fig. 1. (a) Schematic illustration for the morphological evolution of selenized derivatives of MoO_3@Co-MOF precursors with different time of Co-MOF growth. SEM images (b-f) and corresponding nitrogen adsorption-desorption isotherms with pore size distribution (g-k) of the selenized derivatives: (a and g) bare $MoSe_2$; (c and h) MCS1; (d and i) MCS3; (e and j) MCS6; and (f and k) MCS12.

that MC-X retained the similar morphology as MoO_3 nanorods, it is reasonable to conclude that the Co-MOF layer were uniformly coated on the surface of MoO_3 nanorods. So, the MoO_3@Co-MOF structure can be illustrated as Scheme 1.

It is interesting that although MoO_3 nanorods and MC-X precursors show similar micro-morphologies, their selenized derivatives show much more different morphology from each other. Fig. 1 shows the schematic illustration for the morphological evolution of their selenized derivatives and the corresponding SEM and bet data. The bare $MoSe_2$ inherited the dense nanorods morphology with a smooth surface from MoO_3, but it also suffered from a severe agglomeration due to the high reaction temperature of 700 °C (Fig. 2**b**). As for the $MoSe_2$@CoSe/N-doped C (denoted by MCS-X (X = 1, 3, 6 and 12) below) samples, Co-MOF coating layer did a great job in separating MoO_3 nanorods and avoiding agglomeration during the selenization process (Fig. 1**c-f**). After 1 h of Co-MOF growth and subsequent selenization process, MCS1 sample retained the separated nanorods morphology except that their surfaces became rougher and coated with lots of small nanoparticles (Fig. 1**c**). As for the MCS3 sample (Fig. 1**d**), the Co-MOF coating layer grew into scatteredly distributed larger nanoflakes instead of uniformly distributed small nanoparticles upon selenization, and the nanorods beneath is still solid. When the Co-MOF growth time further extended to 6 h, the corresponding selenized sample MCS6 has a much more uniformly distributed coating layer of nanoflakes (Fig. 1**e**). Most of these nanoflakes are inserted into the nanorods beneath them, suggesting a stronger interaction between $MoSe_2$ and CoSe coating layer. Furthermore, as shown in Fig. S4, unlike MCS1 and MCS3, sample MCS6 has a hollow nanorod structure (further proved by TEM in the Fig. 3**b**), which favors its applications in sodium ion batteries and hydrogen evolution reaction. Meanwhile, polygonal thin nanoflakes generally grew into hexagonal shape, which is reasonable as CoSe has a hexagonal crystal structure. However, as the growth time being further extended to 12 h, the hexagonal nanoflakes in the selenized sample tend to aggregate together, resulting in a denser coating layer (Fig. 1**f**) as well as a larger size. Furthermore, the BET results (Fig. 1**g-k** and Fig. S5) of the samples also verify the morphology evolution. The N2 adsorption–desorption isotherms and the pore size distributions of them are shown in Fig. 1**g-k**. The optimal

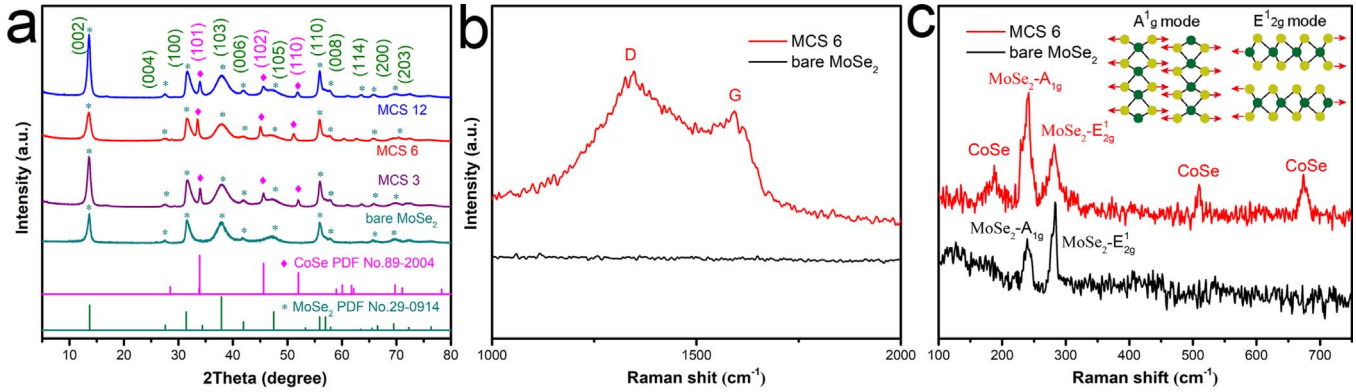

Fig. 2. (a) XRD patterns of MCS3, MCS6 and MCS12 composites; (b and c) Raman spectra of bare $MoSe_2$ and MCS6 composite, inset: illustration of A^1_g and E^1_{2g} mode of $MoSe_2$.

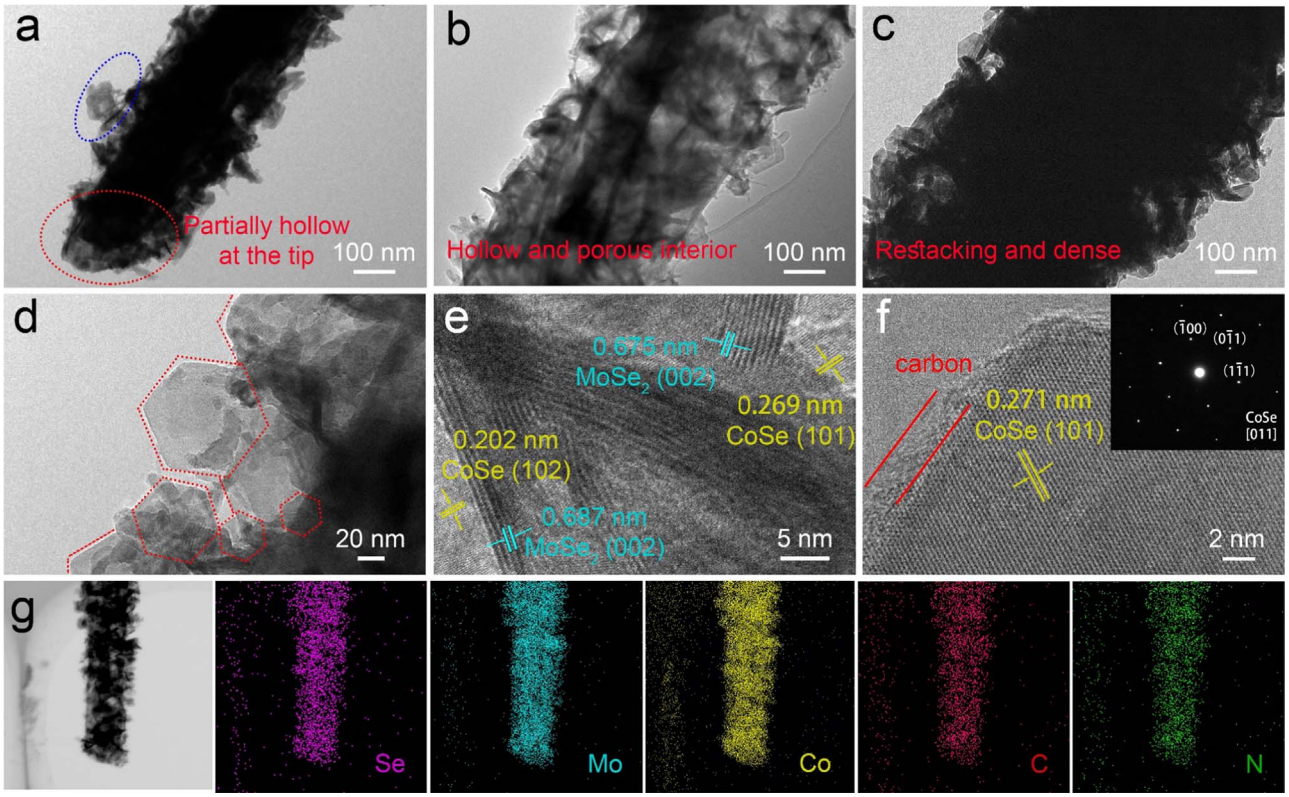

Fig. 3. TEM images of (a) MCS3 composite, (b and d) MCS6 composite, and (c) MCS12 composite; (e and f) HRTEM image of MCS6 composite; (g) elemental mappings (Se, Mo, Co, C and N) of MCS6 composite.

hierarchical composite affords the largest surface area of 35.42 m^2 g^{-1} for MCS6 sample, while for bare $MoSe_2$, MCS1, MCS3, and MCS12, the surface areas are 3.86, 5.46, 12.23, and 13.91 m^2 g^{-1}, respectively. It is clearly seen that the adsorption capacity in low and middle pressure regions increased as the time of Co-MOF growth increased from 0 to 6 h, reflecting ever-growing hierarchical micro–mesopores. Correspondingly, the average sizes of the pores increased from 1 to 4 nm. However, when the time further increased to 12 h, the number of mesopores of around 4 nm decreased. The evolution of morphology demonstrates the essential role played by Co-MOF coating layer in the synthesis of uniform hierarchical nanostructure of hexagonal CoSe nanoflakes on the hollow $MoSe_2$ nanorods.

Bare $MoSe_2$ nanorods, MCS3, MCS6 and MCS12 are picked for further structural study. Firstly, the phase composition of each sample was identified by means of X-ray diffraction (Fig. 2**a**). The strong diffraction peaks located at 13.6°, 31.4°, 37.8°, 47.5°, 55.9°, and 55.9° can be indexed to the atomic planes of (002), (100), (103), (105), (110), and (008) for the hexagonal $MoSe_2$ (JCPDS. 29-0914, 2H-$MoSe_2$), respectively. While those diffraction peaks located at 34.0°, 45.6°, and 52.4° correspond well to the (101), (102), and (110) plane of hexagonal structured CoSe (JCPDS. 89-2004). No other characteristic peaks can be observed suggests the high purity of as-synthesized $MoSe_2$@CoSe/N-doped Carbon (N-C) nanocomposites. The content of $MoSe_2$, CoSe and Carbon in MCS-X samples can be calculated from the ICP and TG results (shown in Fig. S6, Table S1 and Table S2). As the growth time of Co-MOF increases, the content of CoSe increases slightly. And MCS6 sample has the highest carbon content of 16.60%. The presence of $MoSe_2$, CoSe and carbon in sample MCS6 is also confirmed in the Raman spectrum. As presented in Fig. 2**b**, there are two strong peaks at around 1348 cm^{-1} and 1593 cm^{-1}, corresponding to D-band and G-band of carbon, respectively. The I_D/I_G ratio is calculated to be 1.21, demonstrating the amorphous feature of the N doped carbon derived from Co-MOF in MCS6 sample. Meanwhile, Raman spectra in Fig. 2**c** exhibits peaks at around 240 cm^{-1} and 282 cm^{-1}, belonging to the out-of-plane mode (A^1_g) and in-plane mode (E^1_{2g}) of $MoSe_2$, respectively, again implying the 2H-$MoSe_2$ has been synthesized successfully. The A^1_g mode is preferred for edge-terminated $MoSe_2$, whereas the E^1_{2g} mode is favored for terrace-terminated $MoSe_2$, as schematically illustrated in the inset of Fig. 2**c** [51]. Compared to the pure $MoSe_2$, MCS6 sample shows a higher A^1_g/E^1_{2g} intensity ratio, suggesting MCS6 sample has more active edge sites, which can store more Na ions [44]. And peaks at around 191 cm^{-1}, 510 cm^{-1} and 674 cm^{-1} in MCS6 sample belong to CoSe, verifying the successful combination of $MoSe_2$ and CoSe.

TEM was employed to further investigate the influence of Co-MOF growth time on the nanostructures of derived selenide composites, and the results are shown in Fig. 3. With same magnification, Fig. 3**a-c** confirm the increasing trend of diameters from MCS3 to MCS12, which has also been revealed by SEM images discussed above. Take a closer look at Fig. 3**a**, it can be noticed that at the tip of the MCS3 composite (marked by red circle), a hollow structure has formed, while the main body of the nanorod still remains solid. As for the coating nanoflakes, they are unevenly attached to the nanorod substrate and can be easily distinguished from it (marked by blue circle). Fig. 3**b** reveals that the entire nanorod substrate in sample MCS6 became hollow and porous with homogeneous hexagonal nanosheets (can be clearly seen in Fig. 3**d**) uniformly inserted in it. And the interaction between the coating nanoflakes and the substrate is much stronger than that of sample MCS3. The increased size of MCS12 sample (Fig. 3**c**) can be attributed to the thick outer layer of CoSe, which can be proved by Fig. S7 and Fig. S8. In addition to larger size, the restacking and aggregating of these excess CoSe nanosheets also results a denser structure in the MCS12 sample. High-resolution TEM (HRTEM) and selected area electron diffraction (SAED) techniques were also employed to get more detailed structural information of MCS6 sample. Fig. 3**e** reveals the presence of $MoSe_2$ in the coating layer of CoSe, forming a heterostructure of $MoSe_2$ and CoSe. The interlayer distances of 0.687, and 0.675 nm marked in the image all correspond to the d-spacing of (002)

plane of 2H phase $MoSe_2$, which are expanded a little compared to the data from standard pdf card (JCPDS. 29-0914). As a layer structured material connected by weak Van der Waals' force, the expanded *d*-spacing of $MoSe_2$ has also been observed in many works [27,42]. And the fringe spacing of 0.202 and 0.269 nm correspond to the planar distances of (102) and (101) of CoSe, respectively. This expanded interlayer spacing would facilitate the insertion/extraction of Na^+ upon cycling, thus improving its rate capability. The HRTEM image (Fig. 3**f**) of the single hexagonal nanosheet (a thickness of about 6 nm and a side length of about 50 nm) displays the observed fringe spacing of 0.271 nm, corresponding to the planar distances of (101) of CoSe. The SAED pattern of the hexagonal nanosheet shows the single crystal structure. The crystal lattices can be attributed to the [011] diffraction. Moreover, the nanosheet are covered by a carbon layer (marked by red lines), which can facilitate the electron transportation. The dark-field scanning TEM (STEM) graph and corresponding energy dispersive X-ray (EDX) elemental mapping results of MCS6 are disclosed in Fig. 3**g**, which distinctly evidence the uniform distribution of Mo, Co, Se, C and N ingredients. It can be seen that the width of the Co element distribution is larger than that of the Mo element, which again proves that the CoSe is coated outside on $MoSe_2$. Based on the above analyses, it can be concluded that a uniform hierarchical mesoporous $MoSe_2$@CoSe/N-C nanostructure was successfully formed in MSC6 sample.

The formation of the hollow interior in MCS6 sample can be explained by the diffusion-controlled process or Kirkendall effect. On one hand, owing to the abundant selenium around the external Co-MOF coating layer and high surface energy, the selenium tends to react with Co-MOF on the exterior surface first rather than the MoO_3 nanorods covered beneath. On the other hand, MoO_3 have to break strong Mo-O bond before being able to react with selenium and form $MoSe_2$, which makes MoO_3 in an even more unfavorable position than Co-MOF in reacting with selenium [50]. Thus, in order to form $MoSe_2$, internal Mo has to wait until the external Co-MOF gets fully reacted and in the meantime, diffuses outward to meet with the rest of selenium that has travelled through and already partly consumed by the Co-MOF shell. As a result, the $MoSe_2$ formation on the surface of the nanostructure accompanied by the consumption of interior MoO_3 [30]. The difference of diffusion flux can create a gap between the exterior shell and interior, forming a porous structure. Consequently, interesting hierarchical $MoSe_2$@CoSe/N-C nanostructure, with a hollow cavity, was obtained. As for the MCS1 sample, because the Co-MOF coating layer was too thin to block MoO_3 and selenium from each other, which led to a dense interior of $MoSe_2$ nanorod. When the Co-MOF coating layer gets thicker as growth time prolongs, the Kirkendall effect first became noticeable in sample MCS3 (evidenced by the hollow tip, Fig. 3**a**) and came to an optimal degree in sample MCS6 (Fig. 3**b**). However, when the Co-MOF coating layer became even thicker, the derived CoSe/C nanoflakes of sample MCS12 started to stack and overlay with each other and formed a dense coating shell outside the $MoSe_2$, burying the hollow $MoSe_2$ interior and its merits underneath.

Chemical compositions of MCS6 sample are further investigated by X-ray photoelectron spectroscopy (XPS) analysis (Fig. 4). The survey spectrum confirmed the existence of Mo, Co, Se, C, N and O elements (Fig. 4**a**). The presence of O can be attributed to air or methyl alcohol added during the synthesis of MoO_3@Co-MOF. The spectrum shows two peaks at 228.6 and 231.8 eV that can be assigned to Mo $3d_{5/2}$ and Mo $3d_{3/2}$, respectively, indicating the existence of Mo^{4+} (Fig. 4**b**) [27]. For the Co 2p (Fig. 4**c**), the spectrum can be deconvoluted into two spin–orbit doublets and two shakeup satellites (denoted by 'Sat.'). Two peaks located at around 782.1 and 793.5 eV can be assigned to Co $2p_{3/2}$ and Co $2p_{1/2}$, respectively, corresponding to the spin-orbit characteristic of Co^{2+} [26,40,50]. And peaks at 786.6 and 797.2 eV are attributed to the corresponding satellite peaks. By the way, Mo/Co has an atomic ratio of 1.9 in MCS6 composite (Table S3). The 3d peak of Se^{2-} (Fig. 4**d**) can be split into well-defined $3d_{3/2}$ and $3d_{5/2}$ peaks at 55.2 and 54.2 eV. The C 1s spectrum displayed in Fig. 4**e** can be split into three peaks located at 284.6, 285.6, and 287.5 eV, correspond to the sp^2 C, N-sp^2 C, and N-sp^3 C bond [50], respectively, suggesting the successful nitrogen doping of the carbon. According to the relative atomic ratio of C and N, the carbon and nitrogen content in MCS6 sample is calculated to be 9.27% and 0.33% (Table S3), respectively. The doped nitrogen can improve the electronic conductivity of carbon. As shown in Fig. 4**f**, the doped N element can be identified as three different nitrogen species, pyridinic-N at 397.3 eV, pyrrolic-N at 399.0 eV, and graphitic-N at 400.6 eV [27]. Pyridinic-N and pyrrolic-N are more favorable because they can create numerous extrinsic defects and active sites [50]. By the way, the strong peak at 394.5 eV in this spectrum comes from Mo $3p_{3/2}$ [27].

2.2. Electrochemical Na-ion storage performance and reaction kinetics

The sodium storage properties of the $MoSe_2$@CoSe/N-C nanocomposite were evaluated. Fig. 5**a** shows the cyclic voltammogram (CV) curves of sample MCS6 for the initial three cycles at a scanning rate of 0.1 mV S^{-1}. In the first cathodic sweep, four reduction peaks centered at 1.14, 0.87, 0.66 and 0.43 V can be observed. These peaks are all typical and well documented for $MoSe_2$ and CoSe in SIBs [16,26,27,50]. The weak peak at 1.14 V can be associated with the intercalation of Na^+ ions into $MoSe_2$, leading to the formation of Na_xMoSe_2, while the peak at 0.87 V corresponds to the intercalation of Na^+ into CoSe. The intensive peak at 0.66 V could be correlated with the further reduction of both Na_xMoSe_2 and Na_xCoSe into metallic Mo, Co and Na_2Se. The peak around 0.43 V also corresponds to the conversion reaction from Na_xMoSe_2 to metallic Mo and Na_2Se. In addition to intercalation and conversion reactions mentioned above, the formation of a solid electrolyte interface (SEI) layer also contributed to these peaks. In the subsequent anodic sweep, there is a broad peak at 1.81 V, accompanied with a shoulder peak at 2.15 V, corresponding to the oxidation of metallic Mo and Co. After the first cycle, those cathodic peaks noticed in the first cycle were gone and replaced by two less intensive peaks located at 1.09 and 1.38 V, corresponding to the reduction of Co and Mo ions, respectively. The composite electrode showed large irreversible capability loss in the initial cycle, which can be attributed to the irreversible phase transition and the formation of solid electrolyte interface (SEI) layer. No obvious current decay was observed for the subsequent cycles, indicating high reversibility and cycling stability of the MCS6 electrode in sodium storage.

The galvanostatic cycling test was also carried out to further evaluate the composites' long-term cycling performance, all tests were done within the voltage window of 0.01–3.0 V vs Na^+/Na. Fig. 6b shows the discharge/charge curves of selected cycles of the MCS6 sample when cycled at a current density of 0.1 A g^{-1}. The plateaus in these curves are well consistent with the cathodic/anodic peaks observed in CV curves. The discharge and charge capacities in the first cycle were 557 and 452 mAh g^{-1}, respectively, corresponding to a coulombic efficiency (CE) of 81.1%, which climbed to as high as 94.9% in the 2nd cycle and kept high throughout the test. The capacity loss of the initial cycle may come from the trapping of Na^+ ions as well as the formation of a SEI film [27,34]. Except for the initial discharge curve, all the other discharge–charge curves were highly overlapped, indicating a relatively stable SEI layer was formed as well as the superior cycling stability and reversibility of MCS6 electrode.

Fig. 5**c** compares the cycling performances of the bare $MoSe_2$ and MCS-X (X=3, 6, 12) electrodes at the current density of 0.1 A g^{-1} between 0.01 and 3 V vs Na^+/Na. MCS6 and MCS12 exhibit comparable reversible capacities of around 485 mA h g^{-1}, while MCS3 only delivers 430 mA h g^{-1}, but is still higher than that of pure $MoSe_2$, barely over 355 mAh g^{-1}. Besides, all three MCS-X samples have shown great cycling stability throughout the 100-cycle test, whereas the bare $MoSe_2$ starts to decay at the 60th cycle. This result demonstrates that constructing $MoSe_2$ within the CoSe/N-C can indeed improve the

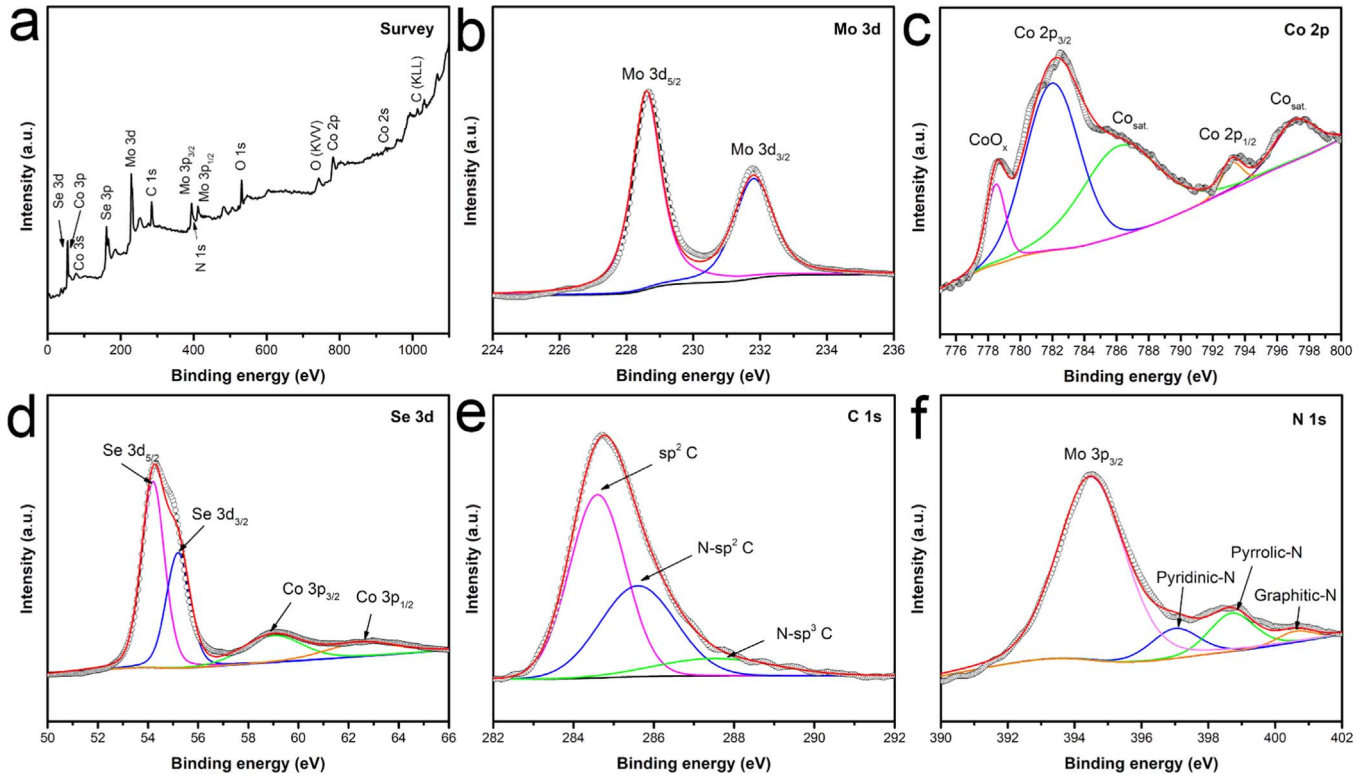

Fig. 4. XPS spectra of MCS6: (a) survey spectrum, (b) Mo 3d, (c) Co 2p, (d) Se 3d, (e) C 1s, and (f) N 1s.

capability of storing Na^+ as well as the cycling stability. The rate performance was also investigated to further evaluate the sodium storage performance of the as-prepared $MoSe_2$@CoSe/N-C composites. As shown in Fig. 5**d**, MCS6 sample exhibits excellent rate performance due to its unique hierarchical and porous structure. Specifically, the average capacities delivered by MCS6 are 445.7, 440.0, 430.3, 410.5, 399.0, and 392.8 mA h g^{-1} when cycled at the current densities of 0.1, 0.2, 0.5, 1.0, 1.5 and 2.0 A g^{-1}, respectively. As for the MCS12 electrode, although it exhibits a comparable specific discharge capacity to that of MCS6 at a moderate cycling rate of 0.1 A g^{-1}, same as it does in the long-term cycling test presented in Fig. 5**e**, it falls much more behind MCS6 at higher current densities. Similarly, MCS3 and bare $MoSe_2$ also suffer from more obvious capacity loss at higher cycling rates. When the current density is switched back to 0.1 A g^{-1} again, reversible specific capacities of MCS-X nano-composites can be recovered to their initial ones, demonstrating the superior cycling stability of the as-synthesized $MoSe_2$@CoSe/N-C composites. Fig. 5**e** compares the long-term cycling performances of MCS-X and bare $MoSe_2$ at a current density as high as 2 A g^{-1}. It can be seen that MCS6 exhibits a great cycling stability that no obvious capacity loss can be observed throughout the test and a high discharge capacity of 347 mAh g^{-1} is retained after 300 cycles with a CE of about 93.3%. As for MCS3 and MCS12 electrodes, capacity retentions after 300 cycles are 79.8% and 20.3%, respectively. Bare $MoSe_2$, on the other hand, undergoes a dramatically capacity fading after 60 cycles. In addition, compared to the CoSe/N-C derived from ZIF-67 [50], MCS-X samples show lower capacities but much better stability during cycling. The lower capacity may be attributed to the low content of CoSe (20.94% in MCS6 sample).

To gain insights on electrochemical reaction kinetics, electrochemical impedance spectra (EIS) and galvanostatic intermittent titration technique (GITT) were measured. As shown in Fig. 5**f**, all Nyquist plots consist of a depressed semicircle in the high frequency region and a straight line in the low frequency region. All plots were well fitted using an equivalent circuit shown in the inset of Fig. 5**f**, where R_{ct} stands for the charge-transfer resistance at the electrode/electrolyte interface and Z_w is the Warburg impedance related to the diffusion of sodium ion in the electrode material [52,53]. Simulated data is given in Table S4. The R_{ct} of MCS6 and MCS12 electrodes are 277.9 and 240.8Ω, respectively, which are smaller than those of their counterparts, confirming that the nitrogen-doped carbon can effectively enhance the kinetics of electronic transportation in the electrode. According to Eq. (S1) (Supporting information), the Na^+ diffusion coefficient of the electrode is inversely proportional to σ, the slope of the line Z′ versus $\omega^{-1/2}$ in low-frequency region [54]. As shown in Fig. 5**g**, the MCS6 electrode has the minimum slope values, which means the largest Na^+ diffusion coefficient. The Na^+ diffusion coefficients of these electrodes during cycling process were further calculated by GITT. Fig. 5**h** and Fig. S9–10 show GITT curves of MCS6 electrode and the corresponding Na^+ diffusion coefficient. The diffusion coefficient of MCS6 electrode is about 2.7510^{-10} to 7.6310^{-11} cm^2 S^{-1}, three times as high as that of bare $MoSe_2$ electrode. This result is consistent with the EIS test. The higher Na^+ diffusion coefficient of MCS6 can be attributed to its optimal hierarchical and porous structure, which shortens the solid-phase diffusion length, resulting in the better rate capability.

These electrochemical test results along with the micro-morphology analyses presented above demonstrate that wrapping up $MoSe_2$ nanorods with CoSe/N-C nanoflakes coating layer does greatly improve the electrochemical performance of as-prepared electrodes. This enhancement can be ascribed to the improved conductivity brought by the N-C network derived from Co-MOF as well as the synergistic interactions between $MoSe_2$ and CoSe. In addition, thin hexagon CoSe nanosheets and edge-rich $MoSe_2$ with expanded interlayer spacing can store more Na^+ and facilitate their diffusion in the interlayer. Moreover, by tuning the growth time to get a Co-MOF coating layer with a proper thickness, the as-synthesized MCS6 sample was able to form a unique hierarchical and porous hybrid nanostructure after selenized, which can even further boost the rate performance by shortening the diffusion path of Na^+. Such a hierarchical and porous structure also benefits the stability of the electrode during cycling by mitigating volume expansion. For verification, micro-morphology (Fig. S11) of MCS6 composites after 50th cycle (fully charged state) was

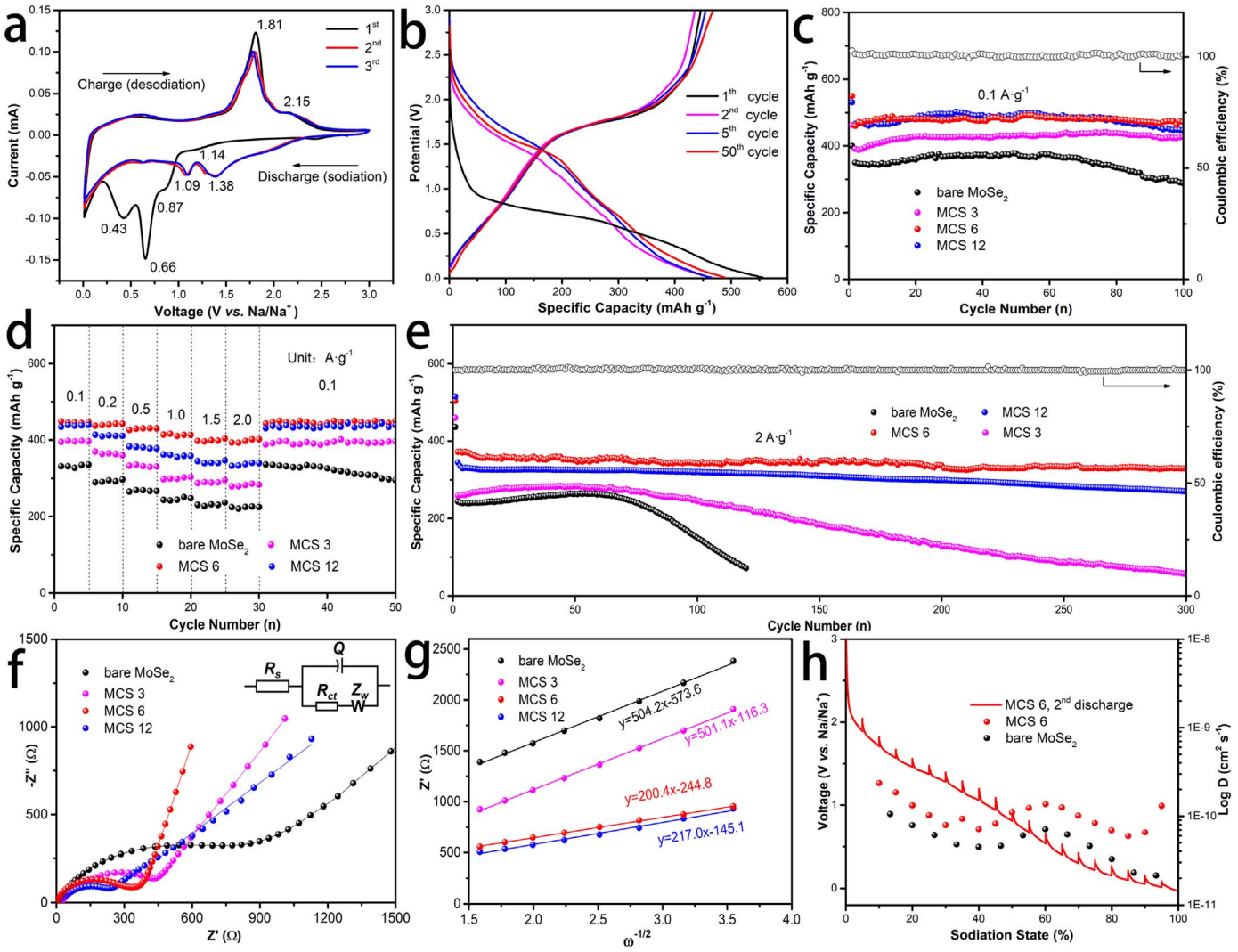

Fig. 5. (a) The first to third cyclic voltammograms of the MCS6 electrode at a scan rate of 0.1 mV s^{-1}; (b) Typical discharge-charge voltage profiles of the MCS6 electrode at a current density of 0.1 A g^{-1}. (c, d and e) Cycling performance and rate performances of bare $MoSe_2$ and MCS-X samples; (f) Nyquist plots for the electrodes made of bare $MoSe_2$ and MCS-X composites, the inset shows the equivalent circuit; (g) The relationship plot of Z' versus $\omega^{-1/2}$ at low-frequency region; (h) GITT curves of MCS6 electrode and the corresponding Na^+ diffusion coefficient of MCS6 and bare $MoSe_2$ electrode.

observed. The morphology of electrode materials remained after cycling, which proves its good structural stability. Besides, longer Co-MOF growth time led to a stronger synergistic interaction between CoSe and $MoSe_2$ in the final product, which also played a positive role in improving the electrochemical performance of MCS6. However, when the Co-MOF growth time was further extended to 12 h, the derived CoSe coating layer became so thick that it not only hindered the fast diffusion of Na^+ but also buried the heterostructure of CoSe and $MoSe_2$ underneath and undermined the synergistic interaction, leading to inferior rate performance compared to that of MCS6.

To verify the practical application of $MoSe_2$@CoSe/N-C nanocomposite, sodium-ion full-cell (NVP/C||MCS6) was assembled (Fig. 6**a**) by employing $Na_3V_2(PO_4)_3$/C cathode reported by our group [54], with the capacity ratio of 1.2:1 between the $Na_3V_2(PO_4)_3$/C cathode and

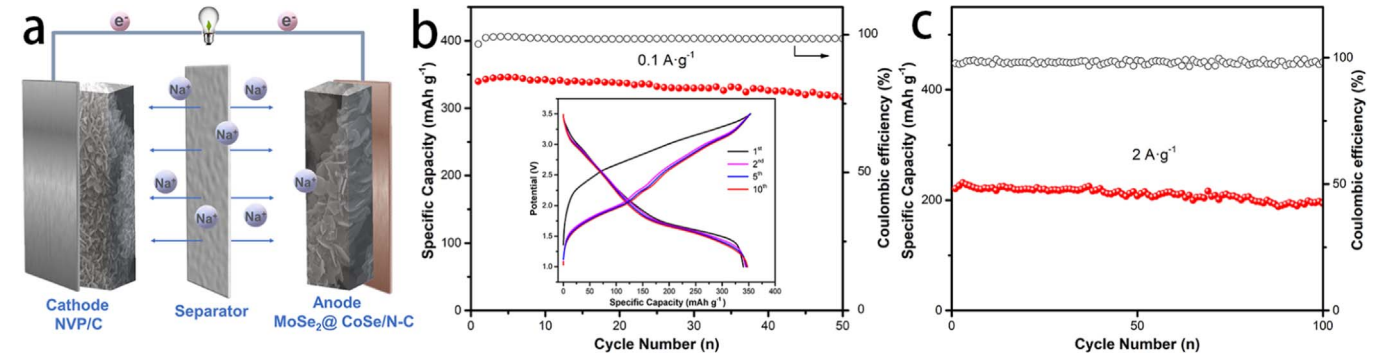

Fig. 6. Sodium-ion full-cell electrochemical performance. (a) Schematic of $Na_3V_2(PO_4)_3$||$MoSe_2$@CoSe/N-C (MCS6) full-cell; (b) capacity retention at 0.1 A g^{-1} and inset: discharge/charge profiles of full-cell, and (c) long cycling performance at 2 A g^{-1} of full-cell.

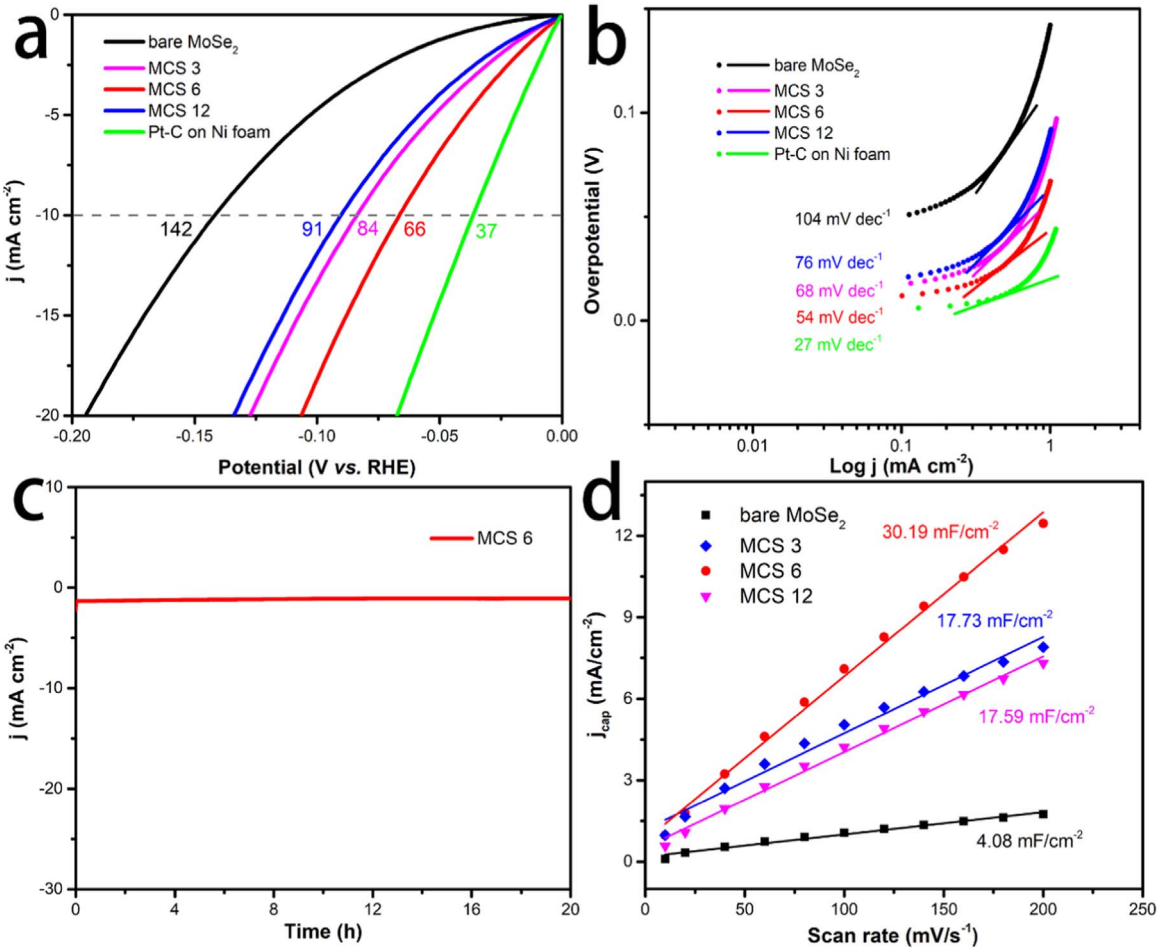

Fig. 7. (a) Polarization curves and (b) Tafel plots of bare $MoSe_2$, MCS3, MCS6, MCS12 and Pt/C for HER in 1 M KOH. (c) The long-term durability tests of MCS6 at η_{10} = 120 mV. (d) Estimation of C_{dl} by plotting the current density variation against scan rate to fit a linear regression.

MCS6 anode. As shown in Fig. 6**b**, the full-cell displays a high reversible capacity of about 345 mA h g^{-1} at 0.1 A g^{-1} (based on anode active mass only). From the second to the tenth cycle, the charge/discharge curves are almost identical, demonstrating a highly reversible charge/discharge behavior. It possesses an average discharge voltage window of 1.41–1.62 V. It also exhibits a good long-term cyclic performance of 197 mA h g^{-1} at 2 A g^{-1} over 100 cycles with an average Coulombic efficiency of above 97.8% (Fig. 6**c**). Such results further support that the $MoSe_2$@CoSe/N-C nanocomposite is a promising anode material for SIBs.

2.3. Electrocatalytic analysis of hydrogen evolution reaction

To further illustrate the multifunctional properties of $MoSe_2$@CoSe/N-C, the electrocatalytic activity (HER) of bare $MoSe_2$ and $MoSe_2$@CoSe/N-C nanohybrids were also studied. The LSV curves of all samples are presented in Fig. 7**a**. In comparison with bare $MoSe_2$, the HER activities of electrodes consist of $MoSe_2$@CoSe/N-C composites are obviously enhanced. The overpotential at 10 mA cm^{-2} (η_{10}) is decreased from 142 mV for bare $MoSe_2$ to 84 mV for MCS3, 66 mV for MCS6, and 91 mV for MCS12. The MCS6 sample exhibits the smallest onset overpotential (η_{10}) among the above samples, only 29 mV larger than that of Pt-C electrode. The Tafel slope can be used to reveal the kinetic information about HER reactions. The smaller Tafel slope reflects more efficient HER kinetics [55]. The linear portions of the Tafel plots (Fig. 7**b**) are fitted to the Tafel equation ($\eta = b \log (j) a$, where η, b and j stand for the overpotential, Tafel slope and current density, respectively). The MCS6 sample shows the smallest Tafel slope of 98 mV dec^{-1}, smaller than those of MCS3 (76 mV dec^{-1}), MCS12 (78 mV dec^{-1}), and bare $MoSe_2$ (117 mV dec^{-1}). Moreover, MSC6 sample also shows lower overpotential and Tafel slope than $CoSe_x$/C derived from Co-MOF [56–58]. The values of the Tafel slopes indicate that the hydrogen evolution over $MoSe_2$@CoSe/N-C samples might be based on the Volmer–Heyrovsky mechanism [59]. Obviously, the MCS6 sample is the most efficient electrocatalyst among them. And it is reasonable to conclude that the distinctive structural advantages possessed by the hierarchical $MoSe_2$@CoSe/N-C nanocomposite is the key reason for achieving an improved HER performance. Firstly, in comparison with bare $MoSe_2$ and the other $MoSe_2$@CoSe/N-C nanocomposite, the MCS6 sample exhibits a notably increased surface area (Fig. 1 and Fig. S5) due to its porous nanorod structure of $MoSe_2$ and uniform nanosized CoSe hexagons. The higher surface area will remarkably facilitate HER performance by exposing more active sites and accelerating mass transfer. Secondly, the hexagonal CoSe and N-doped C can not only provide more active sites, but also greatly enhance the electrical conductivity of the composites, which can be proved by Fig. S12. The high electrical conductivity of the electrode can boost the charge separation efficiency, which in turn enhance HER performance [22]. Moreover, the synergistic effect between the CoSe/C and $MoSe_2$ could accelerate the electron transfer and further heighten the relative catalytic activities. With the best morphology, sample MCS6 is able to expose more $MoSe_2$/CoSe heterostructures on the surface, which enables them to contact with electrolyte to maximize synergistic effect. Thirdly, compared to the bare $MoSe_2$, the ratio of edge-terminated $MoSe_2$ in the MCS6 composite was increased (Fig. 2**c**). As explained for the case of electrocatalysis, the catalytically active sites of $MoSe_2$ tend

to locate at the edges, and thus, the MCS6 composite can provide more active edge sites. Additionally, the porous interior structure is conducive to fast reaction kinetics by promoting the diffusion and penetration processes of reactants.

To further evaluate the electrochemically active surface area (ECSA) of all samples, the electrochemical double layer capacitance (C_{dl}) was obtained by calculating the slope from the linear relationship of the current density against the scan rate in CVs (Fig. S13) within a voltage range from 0.2 to 0.3 V at various scan rates [32]. Calculated C_{dl} values of bare $MoSe_2$ and MCS-X (X = 3, 6 and 12) are 4.08, 17.73, 30.19, and 17.59 mF cm^{-2} (Fig. 7**d**), respectively, which indeed correspond to their HER activities. C_{dl} values of $MoSe_2$@CoSe/N-C nanocomposites imply that the MOF derived CoSe/N-doped C can improve the activity of electrocatalytic active sites in these hybrid catalysts, which is coincident with the improved catalytic performance. The largest C_{dl} is possessed by MCS6 sample, which indicates it has the best exposure and utilization of electroactive sites. Except for the HER activity, the durability is another major concern for electrocatalyst. As shown in Fig. 7**c**, the durability test of MCS6 sample was also conducted by the current density–time curve test at 0.20 V vs RHE. The current density with no significant changes within 20 h of continuous operation indicates the excellent catalytic stability of the $MoSe_2$@CoSe/N-C nanohybrids for HER.

3. Conclusion

In summary, $MoSe_2$@CoSe/N-C tri-composite was synthesized by selenization of MoO_3@Co-MOF nanorods. And the morphology of composite was successfully controlled by adjusting the time duration of Co-MOF growth in the preparation of precursors. In particular, hierarchical and mesoporous structure was obtained in MCS6 sample. Owing to the optimized structure, when evaluated as an anode material for sodium-ion batteries, the MCS6 composite showed high capacity (485 mA h g^{-1} at 0.1 A g^{-1}), outstanding rate properties (398 mA h g^{-1}at 2 A g^{-1}), and long cycle life (91.4% initial capacity retention after 300 cycles at 2 A g^{-1}). Moreover, it also shows promising potential in full-cell configuration. In addition, MCS6 composite also exhibits an excellent HER performance with small overpotentials of 64 mV and Tafel slope of 53 mv dec^{-1}. The good electrochemical performances are attributed to high electronic conductivity contributed by N-C, synergistic advantages between $MoSe_2$ and CoSe, enhanced electrocatalytical activity and less Na^+ diffusion resistance due to large electrode-electrolyte contact area, and alleviated volume change realized by unique hierarchical mesoporous nanostructure. Our work demonstrates that the composite with selected component and hierarchical mesoporous structure is favorable for improving the electrochemical performance in energy storage and conversion applications.

Acknowledgments

This work was supported by the National Natural Science Foundation of China (No 51872334, 51572299), the Program for New Century Excellent Talents in University (No. NCET-13-0594), and the Innovation-Driven Program of Central South University (No. 2017CX001).

Supporting information

Experimental section, supplementary FT-IR, XRD, SEM, TEM, EDX, EIS, CV, GITT, Tables and equations associated with this article can be found in the online version.

Appendix A. Supporting information

Supplementary data associated with this article can be found in the online version at doi:10.1016/j.ensm.2018.10.019

References

[1] M. Wahid, D. Puthusseri, Y. Gawli, N. Sharma, S. Ogale, Chemsuschem 11 (2018) 506–526.
[2] T. Brezesinski, J. Wang, S.H. Tolbert, B. Dunn, Nat. Mater. 9 (2010) 146–151.
[3] W. Zhang, Z. Wu, J. Zhang, G. Liu, N.-H. Yang, R.-S. Liu, W.K. Pang, W. Li, Z. Guo, Nano Energy 53 (2018) 967–974.
[4] Y. Cao, L. Xiao, M.L. Sushko, W. Wang, B. Schwenzer, J. Xiao, Z. Nie, L.V. Saraf, Z. Yang, J. Liu, Nano Lett. 12 (2012) 3783–3787.
[5] Y. Zheng, Y. Jiao, A. Vasileff, S.-Z. Qiao, Angew. Chem. Int. Ed. Engl. 57 (2018) 7568–7579.
[6] W. Luo, F. Shen, C. Bommier, H. Zhu, X. Ji, L. Hu, Acc. Chem. Res. 49 (2016) 231–240.
[7] X. Zhao, H.-E. Wang, Y. Yang, Z.G. Neale, R.C. Massé, J. Cao, W. Cai, J. Sui, G. Cao, Energy Storage Mater. 12 (2018) 241–251.
[8] Z. Hu, Q. Liu, S.L. Chou, S.X. Dou, Adv. Mater. 29 (2017) 24.
[9] S. Hao, X. Shen, M. Tian, R. Yu, Z. Wang, L. Chen, Nano Energy 41 (2017) 217–224.
[10] D.L. Chao, P. Liang, Z. Chen, L.Y. Bai, H. Shen, X.X. Liu, X.H. Xia, Y.L. Zhao, S.V. Savilov, J.Y. Lin, Z.X. Shen, ACS Nano 10 (2016) 10211–10219.
[11] A. Eftelthari, Appl. Mater. Today 8 (2017) 1–17.
[12] Y. Fang, X.Y. Yu, X.W.D. Lou, Adv. Mater. 30 (2018) 1706668.
[13] Y. Zhang, A. Pan, Y. Wang, X. Cao, Z. Zhou, T. Zhu, S. Liang, G. Cao, Energy Storage Mater. 8 (2017) 28–34.
[14] Y.H. Xu, J.W. Liang, K.L. Zhang, Y.C. Zhu, D.H. Wei, Y.T. Qian, Electrochem. Commun. 65 (2016) 44–47.
[15] M.K. Cheng, J. Liang, Y.H. Lai, L.X. Pang, Y. Liu, J.Y. Shen, J.Q. Hou, Q.L. He, B.C. Xu, J.S. Chen, G. Wang, C. Liu, R. Lortz, I.K. Sou, Nanotechnology 28 (2017) 455601.
[16] H. Liu, H. Guo, B. Liu, M. Liang, Z. Lv, K.R. Adair, X. Sun, Adv. Funct. Mater. 28 (2018) 1707480.
[17] Y. Wan, Z. Zhang, X. Xu, Z. Zhang, P. Li, X. Fang, K. Zhang, K. Yuan, K. Liu, G. Ran, Y. Li, Y. Ye, L. Dai, Nano Energy 51 (2018) 786–792.
[18] Y. Jiao, A. Mukhopadhyay, Y. Ma, L. Yang, A.M. Hafez, H. Zhu, Adv. Energy Mater. (2018) 1702779.
[19] T. Yang, Y. Liu, D. Yang, B. Deng, Z. Huang, C.D. Ling, H. Liu, G. Wang, Z. Guo, R. Zheng, Energy Storage Mater. (2018). http://dx.doi.org/10.1016/j.ensm.2018.05.024.
[20] K. Wang, C. Zhou, D. Xi, Z. Shi, C. He, H. Xia, G. Liu, G. Qiao, Nano Energy 18 (2015) 1–11.
[21] M.-H. Wu, J.-T. Lee, Y.J. Chung, M. Srinivaas, J.-M. Wu, Nano Energy 40 (2017) 369–375.
[22] C.Y. Jian, Q. Cai, W.T. Hong, J. Li, W. Liu, Small 14 (2018) 7.
[23] J. Yin, H. Chen, W. Lu, M. Liu, I.L. Li, M. Zhang, W. Zhang, J. Wang, Z. Xu, P. Yan, W.-J. Liu, S.C. Ruan, Nanotechnology 28 (2017) 484001.
[24] Z.-T. Shi, W. Kang, J. Xu, Y.-W. Sun, M. Jiang, T.-W. Ng, H.-T. Xue, D.Y.W. Yu, W. Zhang, C.-S. Lee, Nano Energy 22 (2016) 27–37.
[25] P. He, Y. Fang, X.-Y. Yu, X.W. Lou, Angew. Chem. Int. Ed. 56 (2017) 12202–12205.
[26] J. Li, D. Yan, T. Lu, Y. Yao, L. Pan, Chem. Eng. J. 325 (2017) 14–24.
[27] F. Niu, J. Yang, N. Wang, D. Zhang, W. Fan, J. Yang, Y. Qian, Adv. Funct. Mater. 27 (2017) 1700522.
[28] Y. Lu, J. Nai, X.W.D. Lou, Angew. Chem. Int. Ed. Engl. 57 (2018) 2899–2903.
[29] H.S. Hou, C.E. Banks, M.J. Jing, Y. Zhang, X.B. Ji, Adv. Mater. 27 (2015) 7861–7866.
[30] X. Zhang, X. Li, J. Liang, Y. Zhu, Y. Qian, Small 12 (2016) 2484–2491.
[31] D. Chao, C. Zhu, P. Yang, X. Xia, J. Liu, J. Wang, X. Fan, S.V. Savilov, J. Lin, H.J. Fan, Z.X. Shen, Nat. Commun. 7 (2016) 12122.
[32] T. Meng, L. Zheng, J. Qin, D. Zhao, M. Cao, J. Mater. Chem. A 5 (2017) 20228–20238.
[33] J. Wan, J. Wu, X. Gao, T. Li, Z. Hu, H. Yu, L. Huang, Adv. Funct. Mater. (2017) 1703933.
[34] J. Zhang, M. Wu, T. Liu, W. Kang, J. Xu, J. Mater. Chem. A 5 (2017) 24859–24866.
[35] H. Tang, K. Dou, C.-C. Kaun, Q. Kuang, S. Yang, J. Mater. Chem. A 2 (2014) 360–364.
[36] W. Zhang, J. Mao, W.K. Pang, X. Wang, Z. Guo, Nano Energy 49 (2018) 549–554.
[37] L. Zhang, T. Wang, L. Sun, Y. Sun, T. Hu, K. Xu, F. Ma, J. Mater. Chem. A 5 (2017) 19752–19759.
[38] X. Zhao, H.-E. Wang, Y. Yang, Z.G. Neale, R.C. Massé, J. Cao, W. Cai, J. Sui, G. Cao, Energy Storage Mater. 12 (2018) 241–251.
[39] X. Wang, B. Zheng, B. Yu, B. Wang, W. Hou, W. Zhang, Y. Chen, J. Mater. Chem. A 6 (2018) 7842–7850.
[40] B. Wang, Z. Wang, X. Wang, B. Zheng, W. Zhang, Y. Chen, J. Mater. Chem. A 2018 (6) (2018) 12701–12707.
[41] P. Ge, C. Zhang, H. Hou, B. Wu, L. Zhou, S. Li, T. Wu, J. Hu, L. Mai, X. Ji, Nano Energy 48 (2018) 617–629.
[42] X. Zhao, W. Cai, Y. Yang, X. Song, Z. Neale, H.-E. Wang, J. Sui, G. Cao, Nano Energy 47 (2018) 224–234.
[43] P. Ge, H. Hou, C.E. Banks, C.W. Foster, S. Li, Y. Zhang, J. He, C. Zhang, X. Ji, Energy Storage Mater. 12 (2018) 310–323.
[44] C. Wang, L. Sun, F. Zhang, X. Wang, Q. Sun, Y. Cheng, L. Wang, Small 13 (2017) 1701246.
[45] P. Ge, H.S. Hou, X.Y. Cao, S.J. Li, G.G. Zhao, T.X. Guo, C. Wang, X.B. Ji, Adv. Sci. 5 (2018) 18.
[46] W.C. Zhang, J.F. Mao, S.A. Li, Z.X. Chen, Z.P. Guo, J. Am. Chem. Soc. 139 (2017) 3316–3319.

[47] S. Dang, Q.-L. Zhu, Q. Xu, Nat. Rev. Mater. 3 (2017) 17075.
[48] F. Zheng, Y. Yang, Q. Chen, Nat. Commun. 5 (2014) 5261.
[49] S. Zheng, X. Li, B. Yan, Q. Hu, Y. Xu, X. Xiao, H. Xue, H. Pang, Adv. Energy Mater. 7 (2017) 1602733.
[50] Y. Zhang, A. Pan, L. Ding, Z. Zhou, Y. Wang, S. Niu, S. Liang, G. Cao, ACS Appl. Mater. Interfaces 9 (2017) 3624–3633.
[51] D. Kong, H. Wang, J.J. Cha, M. Pasta, K.J. Koski, J. Yao, Y. Cui, Nano Lett. 13 (2013) 1341–1347.
[52] H. Liu, B. Liu, H. Guo, M. Liang, Y. Zhang, T. Borjigin, X. Yang, L. Wang, X. Sun, Nano Energy 51 (2018) 639–648.
[53] W. Zhang, W.K. Pang, V. Sencadas, Z. Guo, Joule 2 (2018) 1534–1547.
[54] X. Cao, A. Pan, S. Liu, J. Zhou, S. Li, G. Cao, J. Liu, S. Liang, Adv. Energy Mater. (2017) 1700797.
[55] Y. Sun, C. Wang, T. Ding, J. Zuo, Q. Yang, Nanoscale 8 (2016) 18887–18892.
[56] T.T. Liu, Q. Liu, A.M. Asiri, Y.L. Luo, X.P. Sun, Chem. Commun. 51 (2015) 16683–16686.
[57] C. Sun, Q. Dong, J. Yang, Z. Dai, J. Lin, P. Chen, W. Huang, X. Dong, Nano Res. 9 (2016) 2234–2243.
[58] W. Zhou, J. Lu, K. Zhou, L. Yang, Y. Ke, Z. Tang, S. Chen, Nano Energy 28 (2016) 143–150.
[59] F.X. Ma, H.B. Wu, B.Y. Xia, C.Y. Xu, X.W. Lou, Angew. Chem. Int. Ed. Engl. 54 (2015) 15395–15399.